Effect of the size-selective silver clusters on lithium peroxide morphology in lithium–oxygen batteries

Jun Lu[1], Lei Cheng[2], Kah Chun Lau[2], Eric Tyo[2], Xiangyi Luo[1], Jianguo Wen[3], Dean Miller[3], Rajeev S. Assary[2], Hsien-Hau Wang[2], Paul Redfern[1], Huiming Wu[1], Jin-Bum Park[4], Yang-Kook Sun[4], Stefan Vajda[2,5,6,7], Khalil Amine[1] & Larry A. Curtiss[2,5]

Lithium–oxygen batteries have the potential needed for long-range electric vehicles, but the charge and discharge chemistries are complex and not well understood. The active sites on cathode surfaces and their role in electrochemical reactions in aprotic lithium–oxygen cells are difficult to ascertain because the exact nature of the sites is unknown. Here we report the deposition of subnanometre silver clusters of exact size and number of atoms on passivated carbon to study the discharge process in lithium–oxygen cells. The results reveal dramatically different morphologies of the electrochemically grown lithium peroxide dependent on the size of the clusters. This dependence is found to be due to the influence of the cluster size on the formation mechanism, which also affects the charge process. The results of this study suggest that precise control of subnanometre surface structure on cathodes can be used as a means to improve the performance of lithium–oxygen cells.

[1] Chemical Sciences and Engineering Division, Argonne National Laboratory, Lemont, Illinois 60439, USA. [2] Materials Science Division, Argonne National Laboratory, Lemont, Illinois 60439, USA. [3] Electron Microscopy Center, Argonne National Laboratory, Lemont, Illinois 60439, USA. [4] Department of Energy Engineering, Hanyang University, Seoul 133-791, South Korea. [5] Nanoscience and Technology Division, Argonne National Laboratory, Argonne, Illinois 60439, USA. [6] Department of Chemical and Environmental Engineering, School of Engineering, Yale University, New Haven, Connecticut 06520, USA. [7] Institute for Molecular Engineering, The University of Chicago, Chicago, Illinois 60637, USA. Correspondence and requests for materials should be addressed to S.V. (email: vajda@anl.gov) or to K.A. (email: amine@anl.gov) or to L.A.C. (email: curtiss@anl.gov).

The aprotic Li–O₂ battery is of great interest because of the new concept that it employs for electrical energy storage and the possibility for achieving very high energy densities needed for long-range electric vehicles[1–5]. The Li–O₂ battery is based on the use of an electrochemical transformation, that is, formation of Li–O bonds during discharge and breaking of the bonds during charge to store and release electrical energy. A porous oxygen cathode is used to store the solid products generated from the reaction of Li cations with O_2 during discharge. The exact role of electrocatalysts for oxygen reduction during discharge and oxygen evolution during charge is not well established, although there have been numerous studies. These studies included different carbons[6–8] and polycrystalline metal surfaces such as nanoporous gold[9,10], all of which have a variety of active sites. Other studies have reported supported nanoparticles as electrocatalysts in Li–O₂ cells[11–15]. In addition, during the deposition process of nanoparticles it is possible that small clusters may also be present that are acting as electrocatalysts as has been found in surface reactions involving gold clusters[16]. 'Catalysts' for the oxygen reduction reaction only play a role if the discharge product is soluble allowing the reactants, O_2 and Li^+, access to catalytic sites. If the discharge product is not soluble then catalysts will not play a role in the discharge process[17–19].

Recent advances in the capabilities for depositing metal clusters of exact size and composition provide a new technique to create carefully controlled cathode materials for obtaining insight into the role of specific active sites in Li–O₂ batteries and understanding the role of catalysis. Previously, we have shown that size-selective subnanometre metal atom clusters can be stabilized for heterogeneous catalysis and have dramatically different catalytic properties compared with larger nanoparticles or bulk metal surfaces[20–22]. Size-selective clusters have exhibited superior selectivity and unmatched activity for several key catalytic reactions, such as the oxidative dehydrogenation of propane ($Pt_{6–8}$) (ref. 20) and selective oxidation of propylene (Ag_3, $Au_{5–8}$) (refs 21,22). In addition, our recent work has shown that Pd_6 and Pd_{17} clusters are stable and highly active for electrocatalytic water splitting, while Pd_4 clusters show no activity at all[23]. Thus, it is of interest to use cathode materials on the basis of supported size-selected metal clusters in Li–O₂ cells to determine whether surface species at the subnanometre size level play a role in the discharge and charge process.

To use subnanometre clusters in a Li–O₂ cell for study of their properties during discharge and charge, it is necessary to eliminate defect sites in the carbon cathode from participating in the electrochemical process. We have recently accomplished this through the use of an atomic layer deposition (ALD) coating of aluminium oxide on the carbon surface[15]. The ALD was used to deposit a thin film of alumina on the carbon, which covers regions of the defect sites because of preferential attachment there. Palladium nanoparticles (2–5 nm) were subsequently deposited using ALD on the partially alumina-coated carbon surfaces and tested in Li–O₂ cells. The results from this study[15] showed that the alumina coating prevents decomposition of the ether solvent (tetraglyme) from the surface, a problem with Li–O₂ cells, and also results in a very low charge potential when the Pd nanoparticles are used. However, the non-uniformity of the Pd nanoparticles prevented a clear determination of their exact role in obtaining the low charge potential. In addition, other electrolyte stability issues prevented cycling for more than about 12 cycles.

In the study reported here, we have deposited three different sizes of Ag clusters (3, 9 and 15 atoms) on a carbon cathode with an alumina coating on the defect sites. By combining these well-defined cluster sizes with passivation of carbon defect sites, the resulting cathode architecture provides for a well-characterized material for studying the dependence of discharge on catalyst, which has not been possible in any of the previous studies on Li–O₂ batteries. In this paper, we show, using various characterization techniques, that the silver cluster size has a surprising effect on the morphology of the discharge product and that this is due to the clusters acting as active sites to promote different types of formation mechanisms, which gives rise to differing building blocks that make up the mesoscale assemblies of the lithium peroxide-based discharge product.

Results

Cathode materials. Conductive graphitized carbon (GC) was used as the catalyst support material. The carbon surface was partially coated with Al_2O_3 by ALD, which passivates carbon defect sites[15] and is about 0.5 nm thick. At this thickness, coated carbon is still electrically conductive and can act as a support for the silver clusters. Size-selected Ag_n ($n = 3, 9, 15$) clusters were soft landed on the alumina-coated GC under identical deposition and coverage conditions (corresponding to 12.35% atomic monolayer equivalent, ML, of an ideal smooth surface). The principle deposition technique of size-selected cluster is described elsewhere[20–23] (also see Methods).

The size-selected clusters were characterized as to size and composition on the cathode surface. The coverage of soft-landed clusters was kept low enough (12.35% ML) to prevent agglomeration at room temperature. Evidence for this comes from transmission electron microscopy (TEM) images of the Ag_{15} clusters in Fig. 1, which shows 15 atom clusters (Fig. 1c).
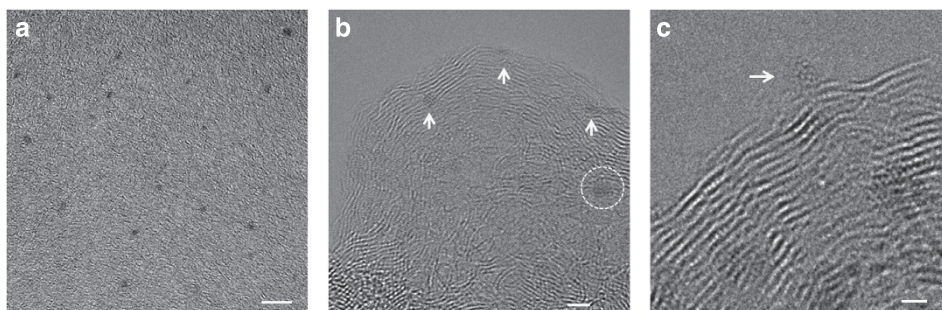
Figure 1 | TEM images of Ag₁₅ clusters on carbon surfaces. (**a**) Low-magnification TEM image of Ag_{15} clusters on an amorphous carbon film showing uniform size and distribution of the clusters (scale bar, 5 nm). (**b**) Medium-magnification TEM image of Ag_{15} clusters (arrows) on an Al_2O_3-coated carbon particle before first discharge. Occasionally, agglomeration of Ag_{15} clusters (large circle) is observed (scale bar, 2 nm). (**c**) High-resolution TEM image of an Ag_{15} cluster on an Al_2O_3-coated carbon surface (scale bar, 1 nm).

The total number of Ag atoms deposited was the same in each case, providing a basis for direct comparison of performance of all cluster sizes. Owing to the same number of atoms deposited, the resulting density of clusters will be different; there will be a higher density of smaller clusters and smaller density of larger clusters. Thus, the results for the three cathodes prepared in this manner provide a precise method to investigate the effect of the metal cluster size and density on the discharge and charge processes in a Li–O$_2$ cell.

The performance of the three silver clusters on the alumina-passivated GC cathode as well as the alumina-passivated GC cathode itself was examined using a Swagelok-type cell[15] composed of a lithium metal anode, electrolyte (1 M LiCF$_3$SO$_3$ in tetraethylene glycol dimethyl ether (TEGDME) impregnated into a glass fibre separator) and a porous cathode (13 mm diameter). A relatively low current density of 100 mA g^{-1} was used for both discharge and charge. Since the same number of Ag atoms are deposited on each cathode surface and the clusters have nearly the same number of surface atoms, the current density will be the same for all three cathodes. Figure 2 shows voltage profiles recorded during the first and second discharge/charge cycles obtained for the three cathode architectures with the three different cluster sizes (Ag$_3$, Ag$_9$, Ag$_{15}$). The discharge product from the Ag$_{15}$-based cathode shows significantly lower charge overpotential (~0.7 eV) compared with that from Ag$_3$ and Ag$_9$ as well as a cathode with no clusters added (see Supplementary Fig. 1). The Li–O$_2$ cell based on the Ag$_{15}$ clusters lasts for about 10 cycles before failing, while the others degrade much faster. The cycling of the Ag$_{15}$ cell for ~10 cycles is evidence for the chemical stability of subnanometre Ag clusters. During charge, the Ag clusters will be oxidized due to their low oxidation potential, but not necessarily become silver oxide since the oxidized clusters are not likely to react with Li$_2$O$_2$ and only react with oxygen over time due to slow reaction kinetics. There are several possible causes for the Ag$_{15}$ cluster cell degradation besides gradual oxidation of the clusters including electrolyte decomposition[24–29] and lithium anode corrosion[30].

Characterization of discharge products. The discharge products resulting from the three cluster sizes were examined using scanning electron microscopy (SEM) and TEM imaging and were found to dramatically depend on the Ag cluster size. The SEM images in Fig. 3 show the carbon cathode after discharge to 2.5 V for the first cycle. The SEM images reveal that the discharge product resulting from the Ag$_3$ cluster-based cathode is film-like. In contrast the discharge product of the Ag$_9$-based cathode is largely toroid-like with rough surfaces, while that of the Ag$_{15}$-based cathode is characterized by toroids with relatively smooth surfaces. The Ag$_9$ toroids are smaller than the Ag$_{15}$ toroids (~500 nm versus ~1,000 nm) with the same discharge capacity. Toroids have been found in the discharge product by others in Li–O$_2$ cells[31–34]. The X-ray diffraction (XRD) patterns in Fig. 3d are consistent with Li$_2$O$_2$ in all three cases. The discharge capacities for the first cycle after discharge to 2.5 V in Fig. 2d also show that the Ag$_{15}$-based cathode capacity (~3,500 mAh g^{-1}) is much larger than those of the Ag$_3$- and Ag$_9$-based cathodes (~2,400 mAh g^{-1}).

The lithium peroxide discharge product on the cathode was further probed by TEM imaging and the results from the first discharge to 2.5 V are shown in Fig. 4. The TEM images show several distinct building blocks that make up the discharge products. A TEM image of a toroid from the discharge product based on the cathode with Ag$_{15}$ clusters is shown in Fig. 4c and indicates the presence of both nanosized grains (nanoparticles of ~10 nm size) and amorphous regions suggesting that the toroids are nanocrystalline, that is, made up of grains and grain boundaries. A higher-resolution TEM image of the Ag$_{15}$ product
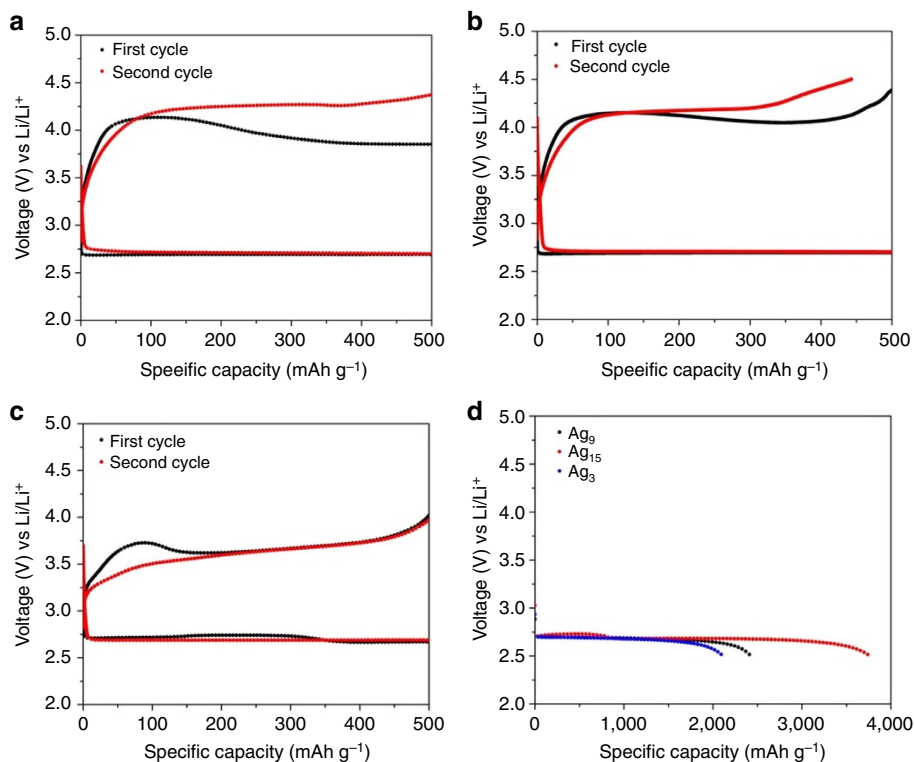

Figure 2 | The first two cycles of capacity-controlled voltage profiles. (a–c) of Li–O$_2$ cells using Ag$_3$-, Ag$_9$- and Ag$_{15}$-based cathode materials; and (d) their first discharge profiles with a cut-off voltage of 2.5 V.
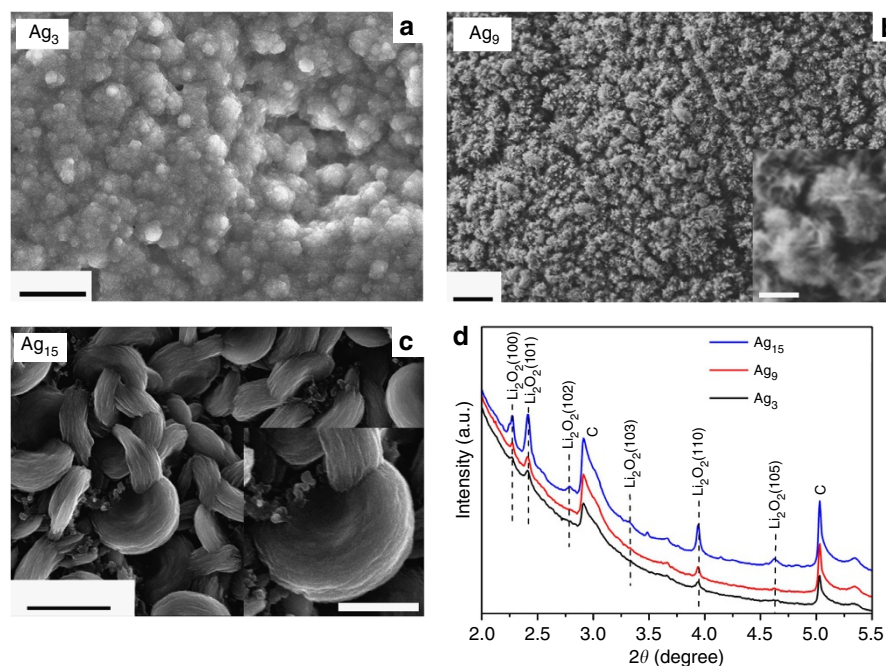
Figure 3 | SEM images and XRD of discharge products. (**a**) on Ag_3-based cathode material (scale bar, 1 μm); (**b**) on Ag_9-based cathode material (scale bar, 1 μm; scale bar of inset image, 250 nm); and (**c**) on Ag_{15}-based cathode material (scale bar, 1 μm; scale bar of inset image, 500 nm). (**d**) XRD patterns for the three discharge products from the three cathode materials. The cells are discharged to 2.5 V in all cases.
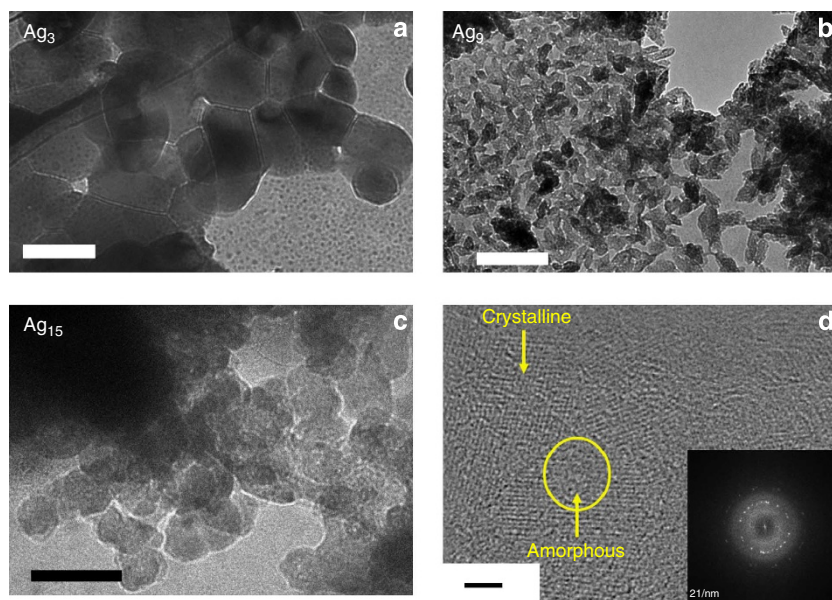
Figure 4 | TEM images of discharge products. (**a**) On Ag_3-based cathode material (scale bar, 200 nm); (**b**) on Ag_9-based cathode material (scale bar, 200 nm); (**c**) on Ag_{15}-based cathode material (scale bar, 20 nm); and (**d**) on Ag_{15}-based cathode material at higher resolution (scale bar, 2 nm). The inset in **d** shows an FFT of the Ag_{15}-based cathode material where the inner ring corresponds to (201) Li_2O_2 planes and the outer ring corresponds to (220) Li_2O_2 planes. Crystalline and amorphous regions are seen in **d**. The cell is discharged to 2.5 V in all cases.

in Fig. 4d also shows amorphous and crystalline regions. The electron diffraction pattern of the Ag_{15} product (Fig. 4d) is consistent with the presence of crystalline Li_2O_2.

The TEM image for the discharge product from the Ag_9-based cathode (Fig. 4b and Supplementary Fig. 2) indicates that its building blocks are elongated nanoparticles or nanorods (~100 nm in length) that are distinctly different from the smaller and more spherical-like nanoparticles found in the discharge product of the Ag_{15}-based cathode. The TEM image of the Ag_3 discharge product in Fig. 4a reveals that it is largely made up of

crystalline flat plates around 50–200 nm in size. Some nanorods are also observed in the Ag_3 discharge product. Electron diffraction patterns and XRD show that the Ag_3 and Ag_9 discharge products contain crystalline Li_2O_2.

Insight into the formation mechanism in the discharge process. The dependence of the morphology of the discharge product on the size of the clusters used for the cathode can be accounted for by two mechanisms involving oxygen reduction and formation of

either LiO_2 or Li_2O_2 in the electrolyte, followed by surface nucleation and growth from the electrolyte. The mechanisms are based on assumptions derived from the characterization evidence and theoretical calculations. The assumptions include, (a) the sites for oxygen reduction and product nucleation are in different locations on the cathode surface; (b) the resulting through-solution mechanism is initiated by desorption of an oxygen superoxide radical anion from the oxygen reduction site; and (c) the electron transfer rate at the oxygen reduction site determines whether the discharge formation is from a mechanism based on surface nucleation from solution of LiO_2 or Li_2O_2. In the following, we present evidence that supports these three assumptions and show how the resulting mechanisms account for the observed morphologies. We note that the dependence on electrolyte is not considered here since the same electrolyte was used for all clusters, but could also be a factor if electrolytes are varied.

The observed building blocks of the discharge product from the cathodes based on the three cluster sizes provide evidence for the first assumption that the formation of the discharge product occurs at a different site than oxygen reduction. Three distinct building blocks (nanorods, plates and ∼ spherical-like nanoparticles) are seen in the TEM images of the discharge product (Fig. 4). If formation of the building blocks occurred at the same site as oxygen reduction, the surface of the discharge product would act as the reduction site and all clusters should result in the same morphology. Thus, the formation process in the case of the Ag clusters is likely occurring by a through-solution process with the oxygen reduction species reaching the nucleation site via the electrolyte. In addition, this implies that desorption of the oxygen reduction product from the active site is necessary to make the site available for further oxygen reduction.

Density functional calculations provide evidence to support the second assumption that oxygen reduction is followed by desorption of the resulting superoxide radical anion into the electrolyte. Density functional calculations (see Supplementary Fig. 3 and Supplementary Table 1) indicate that the O_2^- anion will be weakly adsorbed on an Ag_{15} cluster and, thus, desorption to react with a Li^+ cation to form a solvated LiO_2 molecule will be preferential to Li^+ reaction on the surface to form an adsorbed LiO_2 species. Weak binding of the O_2^- anion is also likely for other possible oxygen reduction sites such as the other clusters or on the cathode surface, and desorption would also occur on these cathodes. Experimental studies have shown that O_2^- anion is soluble in TEGDME-based electrolytes[26]. (Further reduction of the O_2^- anion or LiO_2 is unlikely since it would occur at much lower discharge potential.) Following formation of the solvated LiO_2 molecule, two possible solution phase mechanisms, I and II illustrated in Fig. 5, are possible based on density functional calculations of the free-energy changes. The first three steps of the two mechanisms are the same: oxygen molecule adsorption (A), electron transfer (B) and LiO_2 formation (C). In mechanism I, further solvated LiO_2 formation results in a supersaturated LiO_2 solution (D) and nucleation and growth (E) of LiO_2 at sites on the surface. In mechanism II, reaction of a second superoxide anion and a Li^+ cation with a solvated LiO_2 molecule (step D, Fig. 5) result in a LiO_2 dimer followed by disproportionation to Li_2O_2 (step E) with loss of O_2. This is the only through-solution mechanism for a two-electron reaction to form Li_2O_2 we have found on the basis of the analysis of various reactions (see Supplementary Fig. 4 and Supplementary Table 2). Subsequently, Li_2O_2, after reaching a supersaturated solution (step F), will nucleate and grow on surface sites (step G). There have been other proposed through-solution formation mechanisms[6,35–37], although these have generally assumed that crystal growth occurs in solution. However, homogeneous

nucleation and growth occurring in solution is hard to rationalize because of the different observed building blocks under the same conditions. Likewise, the different building blocks also make it hard to rationalize surface growth of lithium peroxide without solution phase transport of the reduced species for the Ag cluster-based cathodes.

Finally, we address the assumption that electron transfer rate at the oxygen reduction site determines whether the formation mechanism proceeds through mechanism I or II for the cathodes based on Ag clusters. A slow electron transfer rate will cause a slow (solvated) LiO_2 molecule formation rate. This will enable the LiO_2 dimer disproportionation in mechanism II since the half-life of the dimer has very short lifetime[38], and will, thus, lead to heterogeneous nucleation of Li_2O_2 on the cathode surface from a supersaturated solution. Since the building blocks of discharge products based on Ag_3 (plates) and Ag_9 (nanorods) are consistent with possible Li_2O_2 nanoparticle shapes[39,40] they will result from mechanism II. On the other hand, a fast electron transfer rate will favour formation of solvated LiO_2 molecules over dimer disproportionation in solution and result in LiO_2 heterogeneous nucleation as in mechanism I. Since the spherical-like nanoparticle building blocks of the cathode based on Ag_{15} clusters are unlike the other building blocks or what is expected for Li_2O_2, they will result from mechanism I. The spherical particles may also be responsible for the smoother layered-like appearance found in the SEM images (Fig. 3c). Mechanism I involves disproportionation of the solid LiO_2 discharge product on the cathode surface, which appears to contain crystallites, presumably Li_2O_2 and amorphous regions (grain boundaries) of either Li_2O_2 and/or remaining LiO_2 (Fig. 4c,d). The resulting building blocks from the different mechanisms then undergo assembly into mesoscale aggregates that compose the discharge product. The explanation for the toroidal shape of the aggregates is beyond the scope of our model, but a mathematical model[41] has been presented by others on nucleation and conformal growth of Li_2O_2 crystals.

Density functional calculations of the initial nucleation structures of Li_2O_2 on alumina-supported Ag_3 and Ag_9 clusters provide an explanation of the differing building blocks resulting from cathodes based on these two cluster sizes. The results in Fig. 6 indicate that for an Ag_3 cluster, flat $(Li_2O_2)_n$ structures (Fig. 6b) are energetically more favourable (0.49 eV per Li_2O_2 unit) than upright structures (Fig. 6a). This could account for the film-like structure with crystalline plates, which is observed for the discharge product on the Ag_3-based cathode from the TEM results (Fig. 4a). Similar density functional calculations were carried out on alumina-supported Ag_9 clusters. In this case the calculations show that the upright (Fig. 6c) and flat $(Li_2O_2)_n$ clusters are much closer in energy (see Supplementary Fig. 5). This suggests that the three-dimensional Ag_9 cluster could be a nucleation site for the observed elongated nanorod-type Li_2O_2 nanoparticles found in the TEM images (Fig. 4b). We note that, if the clusters act as nucleation sites, the largest toroid size should occur for the cluster size with the lowest cluster density on the surface due to the smaller number of nucleation sites. This is consistent with the largest toroids being found for Ag_{15} clusters (1,000 nm), see Fig. 3, and with smaller toroids (500 nm) for Ag_9 clusters.

Density functional calculations of the electronic structures of the three clusters on a hydroxylated alumina surface also provide a possible explanation for different oxygen reduction rates of the cathodes. The results indicate that both supported Ag_3 and Ag_9 clusters have a gap at the Fermi level (Fig. 6d,e), while Ag_{15} shows no gap at the Fermi level (Fig. 6f). The large difference in density of states suggests that the Ag_{15} site will have more favourable electron transfer than Ag_3 or Ag_9 resulting in the faster LiO_2
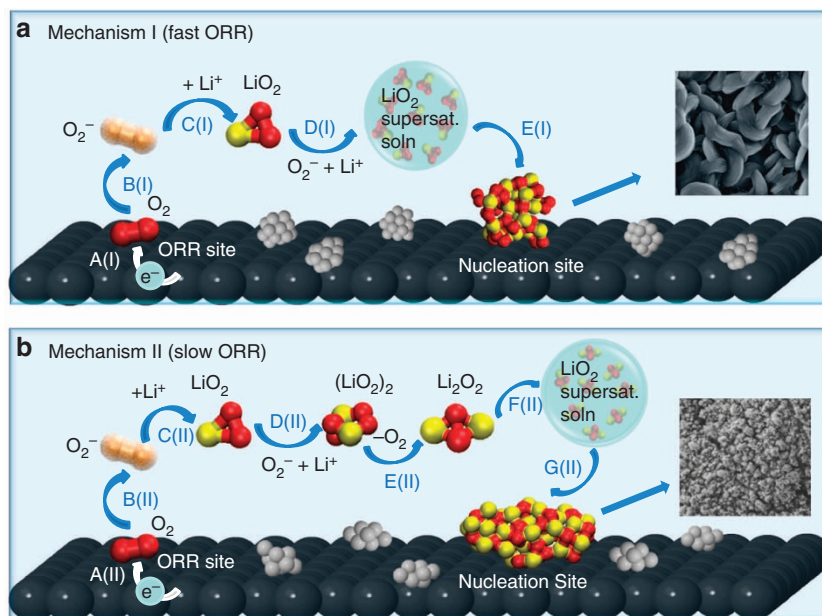
Figure 5 | Proposed reaction mechanisms. Illustration of two discharge reaction mechanisms based on an initial oxygen reduction at an active site followed by solution phase reactions and growth at a surface nucleation site. (**a**) Mechanism I: step A: electron transfer to O_2; step B: O_2^- desorption; step C: Li^+ reaction with O_2^- to form solvated LiO_2; step D: repetition of steps A–C for LiO_2 formation to reach supersaturated LiO_2 solution; step E: surface nucleation and growth of LiO_2 that undergoes disproportionation. (**b**) Mechanism II: step A: electron transfer to O_2; step B: O_2^- desorption; step C: Li^+ reaction with O_2^- to form solvated LiO_2; step D: addition of O_2^- and Li^+ to form LiO_2 dimer; step E: disproportionation to form Li_2O_2 and O_2; step F: repetition of steps A–E for Li_2O_2 formation to reach supersaturated Li_2O_2 solution; step G: surface nucleation and growth of Li_2O_2.
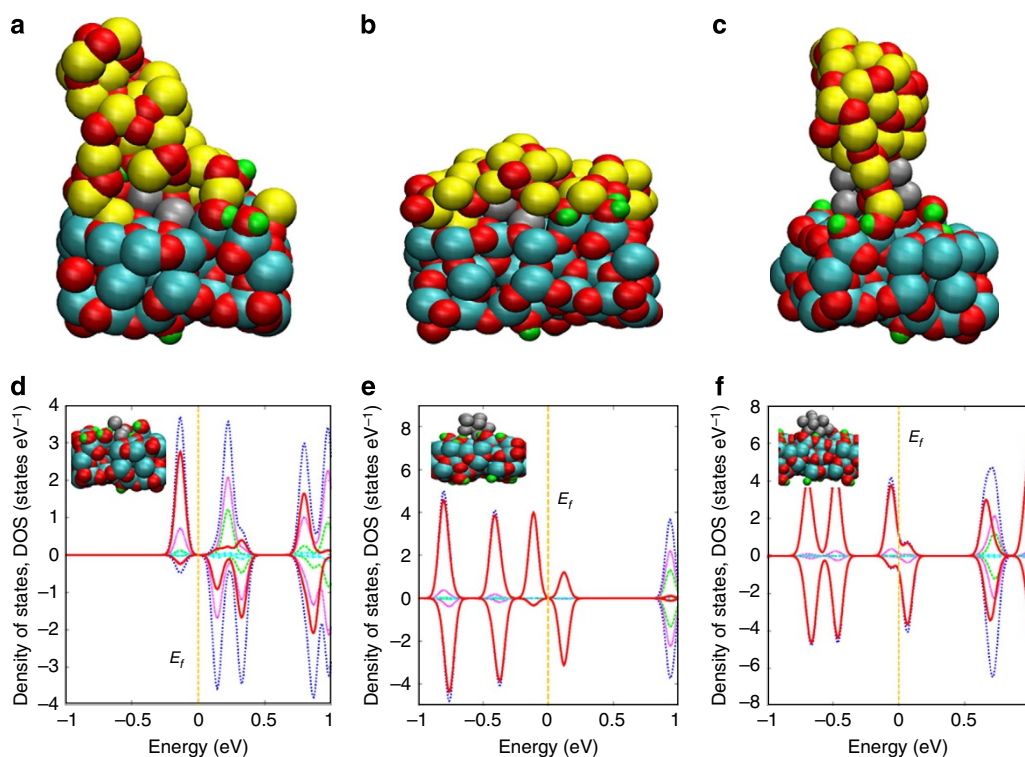
Figure 6 | Density functional studies. (**a**) Lithium peroxide nanorod on an Ag_3 cluster; (**b**) lithium peroxide film on an Ag_3 cluster, which is favoured by 0.49 eV per Li_2O_2 unit compared with the nanorod on an Ag_3 cluster; (**c**) lithium peroxide nanorod on an Ag_9 cluster. Colour code: silver = Ag, blue = Al, red = O and yellow = Li. See Supplementary Fig. 6 for more details on all calculations. (**d**–**f**) Density of states for Ag_3, Ag_9 and Ag_{15} clusters on an amorphous hydroxylated alumina surface.

formation needed for mechanism I. Since the Ag_3 and Ag_9 charge profiles and capacities are similar to those of the alumina-coated carbon cathode without clusters, the oxygen reduction sites are

not likely the clusters in these cases, but rather other cathode surface sites. We also note that the high charge potentials (4 V) for the discharge products from the Ag_3- and Ag_9-based cathodes

(Fig. 2) are consistent with morphologies having poor electronic transport due to larger building blocks (Fig. 4) and lack of a grain boundary network. In contrast, the lower charge potential (~ 0.7 V lower) observed for the Ag_{15}-based cathode is consistent with its smaller nanoparticles and amorphous (grain boundary) network. Such a network could have good electronic conductivity as density functional theory (DFT) calculations[15] have shown that amorphous Li_2O_2 has no band gap. Results for an Ag_{18}-based cathode (see Supplementary Fig. 7) are also consistent with the observed cluster size dependence as the Ag_{18} cluster has a larger band gap and gives results similar (that is, nanorods and large charge potential) to the Ag_9-based cathode.

Discussion

In summary, this study of the Li–O_2 discharge product morphology based on precisely controlled size-selective subnanometre transition metal clusters added to the cathode has revealed a dramatic dependence on cluster size. Such surprising subnanometre size effects have been found recently for other types of electrocatalytic reactions[23,42] as well as heterogeneous catalytic reactions[20–22]. However, this is the first time that size-selected subnanometre clusters have been studied in Li–O_2 cells. The different morphologies of the Li–O_2 discharge products provide evidence, supported by DFT calculations, for discharge mechanisms involving oxygen reduction and formation of either LiO_2 or Li_2O_2 in the electrolyte, followed by surface nucleation and growth from the electrolyte. The dependence of the discharge mechanisms on oxygen reduction rate can account for the differing discharge product morphologies with different charge overpotentials. This study of specific and well-defined clusters on cathode surfaces provides evidence that subnanometre surface species can strongly influence the morphology of the discharge products in Li–O_2 cells. These results imply that characterization of the subnanometre surface structure of cathodes is a key factor in understanding the discharge and charge chemistries in lithium–air cells and the tailoring of this structure is a potential avenue to reduce the charge overpotentials, increase capacities, and possibly increase cycle life with less reactive surface morphologies. It will be of interest to investigate other subnanometre transition metal clusters in Li–O_2 to determine how they control the discharge and charge chemistries.

Methods

Cathode preparation. GC black with a typical particle size 40 nm and a surface area 62 $m^2 g^{-1}$ was used as the catalyst support material. ALD was performed in a continuous-flow stainless steel reactor described in detail elsewhere. About 100 mg of the GC powder was carefully spread onto a stainless steel tray, and a stainless steel mesh cover was clamped over the tray to contain the powder while still providing access to the ALD precursor vapours. The carbon powder was held in the reactor at 200 °C under continuous flow of 300 s.c.c.m. ultra-high-purity nitrogen carrier gas at 1 torr pressure for 30 min to outgas, and achieved thermal equilibrium. The Al_2O_3 ALD used alternating exposures to trimethyl aluminium (TMA, Sigma-Aldrich, 97%) and deionized water at 200 °C. Exposure/purge time 60s-120s-60s-180s was used. The three-cycle Al_2O_3 ALD on the carbon black powder was performed to cover the carbon defect sites. The pristine cathode laminate was formed by casting a mixture of the as-prepared Al_2O_3-coated Super P Li (SPL) carbon and binder in a molar ratio of 80:20. Size-selected Ag_n ($n = 3, 9, 15, 18$) clusters were soft landed on the alumina-coated SPL carbon laminates under identical deposition and coverage conditions (corresponding to 12.35% ML of an ideal smooth surface). In this study, the molecular beam of silver clusters was produced by magnetron sputtering of a silver target using a mixture of argon and helium as the sputtering gas and helium as carrier gas. Next, the charged particles contained in the beam were focused using a conical octupole, passed through a linear octupole ion guide and mass selected by a quadrupole mass filter before the positively charged cluster ions were soft landed on the support. The charge of gas–phase positively charged clusters was neutralized by the current from a picoammeter that is used to bias the support during landing and to monitor the flux of charge in real time on interaction with the conductive support creating a current that is monitored in real time using a picoammeter to determine the coverage flux of particles reaching the support. The amount of deposited metal was

determined by integrating the deposition flux over time (that is, total charge of clusters measured at the surface) and the number of atoms in the cluster.

Electrochemical methods. Electrochemical characterization was carried out using a Swagelok-type cell composed of a lithium metal anode, electrolyte (1 M $LiCF_3SO_3$ in TEGDME impregnated into a glass fibre separator) and a porous cathode (13 mm diameter). The cells were sealed except for the Al grid window that exposed the porous cathode to 1 bar O_2 pressure. The electrochemical measurements were carried out using a Maccor cycler. The discharge–charge performance was conducted at a constant current of 100 mA g^{-1} (carbon), and the cell was maintained in 1 bar O_2 atmosphere to avoid any negative effects of humidity and CO_2. For comparison, a blank Al_2O_3-coated SPL carbon without any catalyst was also tested using the same cell configuration described above. We normalized the observed capacity by the weight of the carbon for comparison in this study.

High-energy XRD. The cathode laminates after discharge were characterized by high-energy synchrotron XRD to determine the formation of Li_2O_2, which was carried out at the 11-ID-C beamline of the Advanced Photon Source, Argonne National Laboratory. The X-ray wavelength was 0.10804 Å. The samples were completely covered with Kapton tape as a protective film in the glove box to avoid any side reactions from the air. The XRD patterns were collected in the transmission mode using a Perkin Elmer large area detector. The collected two-dimensional patterns were then integrated into conventional one-dimensional patterns (intensity versus 2θ) for final data analysis using the Fit2d software.

Electron microscopy. A field-emission transmission electron microscope with a spherical and chromatic aberration imaging corrector working at 80 kV was employed to evaluate the morphology and particle size of the deposited Ag_n clusters and Li_2O_2 toroids. To avoid knock-out damage to carbon materials from the electron beam, 80 kV was chosen. Spherical and chromatic aberration correction enables the microscope to reach the information limit better than 0.1 nm (measured by Young's fringes) at 80 kV. To prepare the TEM specimens, holey carbon grids are placed in the bottle of as-received powders, and shaken to allow small powders to attach on the holey carbon. No liquid was used to avoid possible morphology change due to the interaction with solution. Field-emission SEM (Hitachi S-4700) coupled with energy-dispersive spectrometry was employed to determine the morphology and estimate the particle size of Li_2O_2 toroids.

Theoretical methods. To study the interaction/bindings of the Ag clusters with the alumina surface and the carbon surface, we carried out DFT calculations with plane wave basis sets as implemented in VASP code. More detailed information on the DFT calculations can be found in Supplementary Methods.

References

1. Abraham, K. M. & Jiang, Z. A polymer electrolyte-based rechargeable lithium/oxygen battery. *J. Electrochem. Soc.* **143**, 1–5 (1996).
2. Lu, J. *et al.* Aprotic and Aqueous Li–O_2 Batteries. *Chem. Rev.* **114**, 5611–5640 (2014).
3. Lei, Y. *et al.* Synthesis of porous carbon supported palladium nanoparticle catalysts by atomic layer deposition: application for rechargeable lithium-O_2 battery. *Nano. Lett.* **13**, 4182–4189 (2013).
4. Qin, Y. *et al.* In situ fabrication of porous-carbon-supported α-MnO_2 nanorods at room temperature: application for rechargeable Li–O_2 batteries. *Energy Environ. Sci.* **6**, 519–531 (2013).
5. Du, P. *et al.* Compatibility of lithium salts with solvent of the non-aqueous electrolyte in Li–O_2 batteries. *Phys. Chem. Chem. Phys.* **15**, 5572–5581 (2013).
6. Ottakam Thotiyl, M. M., Freunberger, S. A., Peng, Z. & Bruce, P. G. The carbon electrode in nonaqueous Li–O_2 cells. *J. Am. Chem. Soc.* **135**, 494–500 (2012).
7. Li, Y. *et al.* Carbon black cathodes for lithium oxygen batteries: Influence of porosity and heteroatom-doping. *Carbon* **64**, 170–177 (2013).
8. Xiao, J. *et al.* Hierarchically porous graphene as a lithium-air battery electrode. *Nano Lett.* **11**, 5071–5078 (2011).
9. Peng, Z., Freunberger, S. A., Chen, Y. & Bruce, P. G. A reversible and higher-rate Li–O_2 battery. *Science* **337**, 563–566 (2012).
10. Lu, Y.-C. *et al.* Platinum-gold nanoparticles: a highly active bifunctional electrocatalyst for rechargeable lithium-air batteries. *J. Am. Chem. Soc.* **132**, 12170–12171 (2010).
11. Dathar, G. K. P., Shelton, W. A. & Xu, Y. Trends in the catalytic activity of transition metals for the oxygen reduction reaction by lithium. *J. Phys. Chem. Lett.* **3**, 891–895 (2012).
12. Zhang, Z. C. *et al.* Increased stability toward oxygen reduction products for lithium-air batteries with oligoether-functionalized silane electrolytes. *J. Phys. Chem. C* **115**, 25535–25542 (2011).
13. Débart, A., Paterson, A. J., Bao, J. & Bruce, P. G. α-MnO_2 nanowires: a catalyst for the O_2 electrode in rechargeable lithium batteries. *Angew. Chem. Int. Ed.* **47**, 4521–4524 (2008).

14. Trahey, L. *et al.* Synthesis, characterization, and structural modeling of high-capacity, dual functioning MnO₂ electrode/electrocatalysts for Li-O₂ cells. *Adv. Energy Mater.* **3,** 75–84 (2013).

15. Lu, J. *et al.* A nanostructured cathode architecture for low charge overpotential in lithium-oxygen batteries. *Nat. Commun.* **4,** 2383 (2013).

16. Herzing, A. A., Kiely, C. J., Carley, A. F., Landon, P. & Hutchings, G. J. Identification of active gold nanoclusters on iron oxide supports for CO oxidation. *Science* **321,** 1331–1335 (2008).

17. McCloskey, B. D. *et al.* On the efficacy of electrocatalysis in nonaqueous Li-O₂ batteries. *J. Am. Chem. Soc.* **133,** 18038–18041 (2011).

18. Hummelshoj, J. S., Luntz, A. C. & Norskov, J. K. Theoretical evidence for low kinetic overpotentials in Li-O₂ electrochemistry. *J. Chem. Phys.* **138,** 034703 (2013).

19. Viswanathan, V. *et al.* Electrical conductivity in Li₂O₂ and its role in determining capacity limitations in non-aqueous Li-O₂ batteries. *J. Chem. Phys.* **135,** 214704 (2011).

20. Vajda, S. *et al.* Subnanometre platinum clusters as highly active and selective catalysts for the oxidative dehydrogenation of propane. *Nat. Mater.* **8,** 213–216 (2009).

21. Lei, Y. *et al.* Increased silver activity for direct propylene epoxidation via subnanometer size effects. *Science* **328,** 224–228 (2010).

22. Lee, S. *et al.* Selective propene epoxidation on immobilized Au₆₋₁₀ clusters: the effect of hydrogen and water on activity and selectivity. *Angew. Chem. Int. Ed.* **48,** 1467–1471 (2009).

23. Kwon, G. *et al.* Size-dependent subnanometer Pd cluster (Pd4, Pd6, and Pd17) water oxidation electrocatalysis. *ACS Nano* **7,** 5808–5817 (2013).

24. Freunberger, S. A. *et al.* Reactions in the rechargeable lithium-O₂ battery with alkyl carbonate electrolytes. *J. Am. Chem. Soc.* **133,** 8040–8047 (2011).

25. Mizuno, F., Nakanishi, S., Kotani, Y., Yokoishi, S. & Iba, H. Rechargeable Li-air batteries with carbonate-based liquid electrolytes. *Electrochem.* **78,** 403–405 (2010).

26. Black, R. *et al.* Screening for superoxide reactivity in Li-O₂ batteries: effect on Li₂O₂/LiOH crystallization. *J. Am. Chem. Soc.* **134,** 2902–2905 (2012).

27. McCloskey, B. D. *et al.* Twin problems of interfacial carbonate formation in nonaqueous Li-O₂ batteries. *J. Phys. Chem. Lett.* **3,** 997–1001 (2012).

28. Assary, R. S. *et al.* The effect of oxygen crossover on the anode of a Li-O₂ battery using an ether-based solvent: insights from experimental and computational studies. *ChemSusChem* **6,** 51–55 (2013).

29. Nasybulin, E. *et al.* Effects of electrolyte salts on the performance of Li-O₂ batteries. *J. Phys. Chem. C* **117,** 2635–2645 (2013).

30. Assary, R. S., Lau, K. C., Amine, K., Sun, Y.-K. & Curtiss, L. A. Interactions of dimethoxy ethane with Li₂O₂ clusters and likely decomposition mechanisms for Li-O₂ batteries. *J. Phys. Chem. C* **117,** 8041–8049 (2013).

31. Yang, J. *et al.* Evidence for lithium superoxide-like species in the discharge product of a Li-O₂ battery. *Phys. Chem. Chem. Phys.* **15,** 3764–3771 (2013).

32. Black, R., Lee, J.-H., Adams, B., Mims, C. A. & Nazar, L. F. The role of catalysts and peroxide oxidation in lithium–oxygen batteries. *Angew. Chem. Int. Ed.* **52,** 392–396 (2013).

33. Gallant, B. M. *et al.* Influence of Li₂O₂ morphology on oxygen reduction and evolution kinetics in Li-O₂ batteries. *Energy Environ. Sci.* **6,** 2518–2528 (2013).

34. Adams, B. D. *et al.* Current density dependence of peroxide formation in the Li-O₂ battery and its effect on charge. *Energy Environ. Sci.* **6,** 1772–1778 (2013).

35. Oh, S. H., Black, R., Pomerantseva, E., Lee, J.-H. & Nazar, L. F. Synthesis of a metallic mesoporous pyrochlore as a catalyst for lithium–O₂ batteries. *Nat. Chem.* **4,** 1004–1010 (2012).

36. Ren, X., Zhang, S. S., Tran, D. T. & Read, J. Oxygen reduction reaction catalyst on lithium/air battery discharge performance. *J. Mater. Chem.* **21,** 10118–10125 (2011).

37. Mitchell, R. R., Gallant, B. M., Shao-Horn, Y. & Thompson, C. V. Mechanisms of morphological evolution of Li₂O₂ particles during electrochemical growth. *J. Phys. Chem. Lett.* **4,** 1060–1064 (2013).

38. Bryantsev, V. S., Blanco, M. & Faglioni, F. Stability of lithium superoxide LiO₂ in the gas phase: computational study of dimerization and disproportionation reactions. *J. Phys. Chem. A* **114,** 8165–8169 (2010).

39. Mo, Y., Ong, S. P. & Ceder, G. First-principles study of the oxygen evolution reaction of lithium peroxide in the lithium-air battery. *Phys. Rev. B* **84,** 205446 (2011).

40. Radin, M. D., Rodriguez, J. F., Tian, F. & Siegel, D. J. Lithium peroxide surfaces are metallic, while lithium oxide surfaces are not. *J. Am. Chem. Soc.* **134,** 1093–1103 (2012).

41. Horstmann, B. *et al.* Rate-dependent morphology of Li₂O₂ growth in Li–O₂ batteries. *J. Phys. Chem. Lett.* **4,** 4217–4222 (2013).

42. Proch, S., Wirth, M., White, H. S. & Anderson, S. L. Strong effects of cluster size and air exposure on oxygen reduction and carbon oxidation electrocatalysis by size-selected Ptn (n≤11) on glassy carbon electrodes. *J. Am. Chem. Soc.* **135,** 3073–3086 (2013).

Author contributions

J.L. and K.A. designed the experiments; E.T. and S.V. synthesized the cathode materials. J.L., D.M. and J.W. performed and analysed the imaging experiments, J.L., H.H.W. and X.L. performed and analysed the X-ray measurements, J.L., X.L., J.-B. P. and H.W. tested the cathode materials, and L.C., K.C.L., R.S.A., P.R. and L.A.C. were responsible for the theoretical computations. Y.-K.S., S.V., L.A.C., and K.A. supervised the project; L.A.C., J.L. and K.A. wrote the paper. All of the authors discussed the results and reviewed the manuscript.